



PAPER • OPEN ACCESS

Generation of GHz surface acoustic waves in (Sc,Al)N thin films grown on free-standing polycrystalline diamond wafers by plasma-assisted molecular beam epitaxy

To cite this article: Mingyun Yuan *et al* 2024 *J. Phys. D: Appl. Phys.* **57** 495103

View the [article online](#) for updates and enhancements.

You may also like

- [Etching of Ga₂O₃: an important process for device manufacturing](#)
Zhaoying Xi, Zeng Liu, Junpeng Fang et al.
- [Negative damping of terahertz plasmons in counter-streaming double-layer two-dimensional electron gases](#)
Shengpeng Yang, Hongyang Guo, Ping Zhang et al.
- [Advances in optical recording techniques for non-invasive monitoring of electrophysiological signals](#)
Jiaxin Li, He Ding, Yongtian Wang et al.



ECS The Electrochemical Society
Advancing solid state & electrochemical science & technology

247th ECS Meeting
Montréal, Canada
May 18-22, 2025
Palais des Congrès de Montréal

Showcase your science!

Abstracts due December 6th

Generation of GHz surface acoustic waves in (Sc,Al)N thin films grown on free-standing polycrystalline diamond wafers by plasma-assisted molecular beam epitaxy

Mingyun Yuan^{1,*} , Duc V Dinh¹ , Soumen Mandal² , Oliver A Williams² ,
Zhuohui Chen³ , Oliver Brandt¹  and Paulo V Santos¹ 

¹ Paul-Drude-Institut für Festkörperelektronik, Leibniz-Institut im Forschungsverbund Berlin e.V.,
Hausvogteiplatz 5–7, 10117 Berlin, Germany

² School of Physics and Astronomy, Cardiff University, Cardiff CF24 3AA, United Kingdom

³ Huawei Technologies Co Ltd, Ottawa, Ontario, Canada

E-mail: yuan@pdi-berlin.de

Received 30 April 2024, revised 22 July 2024

Accepted for publication 3 September 2024

Published 16 September 2024



Abstract

Telecommunication of the next generation demands filters that can operate in the 10 GHz range with sufficient bandwidths. For surface-acoustic-wave (SAW) devices this prerequisite translates into high sound velocities and high piezoelectric couplings. Wurtzite AlN on diamond, which exploits the strong piezoelectricity of AlN with the very high SAW velocity of diamond, has been considered a promising platform. A significant boost (up to a factor of 4) of the piezoelectric response can be obtained by alloying AlN with Sc. Here, the main challenge lies in the synthesis of highly-oriented thin (Sc,Al)N films on diamond. In this work, we aim at establishing a platform for SAW devices using plasma-assisted molecular beam epitaxy for the deposition of Sc_{0.2}Al_{0.8}N on diamond. We investigate the structural properties related to SAW generation gearing towards applications at high frequencies. To this end, we prepare (Sc,Al)N thin films on polished polycrystalline diamond wafers and demonstrate the efficient generation of SAW modes with frequencies up to 8 GHz. Systematic studies of the dependence of the SAW velocity and electromechanical coupling coefficient on the Sc_{0.2}Al_{0.8}N film thickness is presented for various SAW modes. Our result demonstrates the potential of this material combination for future application that requires large bandwidth in the ultra-high frequency range.

Keywords: scandium aluminium nitride, surface acoustic waves, diamond, molecular beam epitaxy, GHz waves, Sezawa mode

* Author to whom any correspondence should be addressed.



Original Content from this work may be used under the terms of the [Creative Commons Attribution 4.0 licence](https://creativecommons.org/licenses/by/4.0/). Any further distribution of this work must maintain attribution to the author(s) and the title of the work, journal citation and DOI.

1. Introduction

Future telecommunication technologies require surface-acoustic-wave (SAW) structures yielding high-frequency operation and wide bandwidths. In this context, AlN films grown on diamond is a desirable material combination for several reasons. Wurtzite AlN is a strongly piezoelectric and inherently insulating material, which facilitates the efficient generation of high-frequency SAWs [1]. The piezoelectric response of AlN can be further enhanced by alloying with Sc [2–5], which helps to increase the bandwidth of SAW devices. The AlN/diamond platform supports SAWs with very high propagation velocities, so that resonators in the several GHz range can be fabricated with dimensions well within the resolution of existing nanofabrication technologies. Furthermore, the acoustic velocity of the diamond substrate ($12\,830\text{ m s}^{-1}$, shear vertical [6]) far exceeds the one in the AlN film (6440 m s^{-1} , shear vertical [7]), commonly referred to as ‘slow on fast’. The SAWs are, therefore, effectively waveguided along the film, thus creating favourable conditions for increasing the electromechanical coupling as well as for the excitation of high-order SAW modes. Besides, the AlN/diamond material system is suitable for operation at high power levels as well as high temperatures. Finally, this material combination is also relevant for applications in quantum technologies. Here, one can exploit optically active colour centres in diamond as qubits, whose spin transitions can be induced by SAWs [8]. To access higher-energy transitions and pump higher-frequency single-photon emission, it is desirable to generate SAWs in the multi-GHz range.

SAW devices reported on diamond commonly adopts ZnO as piezoelectric films [9, 10], which have a much lower sound velocity than AlN. Among the existing reports of AlN [11, 12] and (Sc,Al)N [13–15] on diamond, sputtering has been the method chosen for the film growth. Whereas sputtering is very effective in synthesizing films with thicknesses exceeding one μm , the possibility of thinner, submicron films remains a challenge, which hinders the generation of SAWs of higher frequencies. An epitaxial technique such as plasma-assisted molecular beam epitaxy (PAMBE) offers better control and can potentially enhance the film quality. Indeed, (Sc,Al)N films grown on Si(111) by PAMBE have shown improved crystal quality and enhanced performance for SAW applications compared to sputtered material [4, 16]. However, the strong tendency of MBE to perfectly replicate the orientation of the substrate is not advantageous on a polycrystalline substrate as used in the present study. A further challenge is the considerable roughness and waviness of the free-standing polycrystalline diamond substrates.

In this work, we synthesize (Sc,Al)N thin films by PAMBE on chemo-mechanically polished, free-standing polycrystalline diamond substrates. Compared to single-crystal diamond, large area polycrystalline diamond substrates can be synthesized on Si(001) wafers at relatively low costs, thus allowing the scale-up of device processing. We employed films with a nominal Sc concentration of 20% with a thickness of $h = 700\text{ nm}$.

Surface acoustic waves are generated by interdigital transducers (IDTs) covering the frequency range from 2 to 8 GHz, thus enabling us to access the dependence of SAW velocity on the relative ratio between film thickness and the SAW wavelength h/λ_{SAW} . Up to four SAW modes are observed, thus demonstrating the SAW waveguiding along the (Sc,Al)N film. We have performed theoretical calculation of the nominal phase velocity based on the material properties reported in [17], showing good agreement between the experimental and the calculated results. By fitting the Y-parameters to the modified Butterworth van Dyck (BvD) model, the effective electromechanical coupling coefficient k_{eff}^2 has been extracted for different modes over an extended range of normalized thickness h/λ_{SAW} for the nominal Sc concentration. In general, we have obtained $k_{\text{eff}}^2 \sim 1\%$ for the fundamental mode M0. Additionally, a higher mode M3 with k_{eff}^2 of 5% is observed. There is a deviation from the theoretical calculation, which we attempt to explain with the relation between mode distribution and the heterostructure interface.

This report is organized as follows. In section 2, we introduce the processes for growing the diamond substrates and the (Sc,Al)N films. In section 3, we discuss the results of the radio-frequency (RF) generation of SAWs, followed by a comparison with theoretical calculation and BvD fitting in section 4. We summarize the results in section 5.

2. Fabrication of free-standing diamond substrates and MBE growth of (Sc,Al)N

2.1. Fabrication of free-standing diamond substrates

The free-standing polycrystalline diamond layers were synthesised by microwave plasma chemical vapour deposition (MPCVD). A conductive Si(001) wafer was used as a substrate to reduce wafer bow during growth. Due to difference in surface energy between Si and diamond, a seeding technique is needed to form fully coalesced diamond layers [18, 19]. Electrostatic seeding was used to self-assemble high density of seeds on the Si wafer. The seeded wafer was then introduced into a Carat Systems MPCVD system. Diamond was grown using 3% methane in hydrogen. The growth temperature was around 900°C . After the deposition, the diamond layer was cooled to room temperature under hydrogen atmosphere. The Si substrate was then dissolved in an $\text{HF}:\text{HNO}_3:\text{CH}_3\text{COOH}$ (14:5:1) solution to recover a free-standing diamond wafer measuring approximately $150\text{ }\mu\text{m}$ in thickness. The free-standing wafer was then laser diced to create $10 \times 10\text{ mm}^2$ pieces for further processing. The smooth side of the wafer, previously interfacing the Si substrate, was further chemo-mechanically polished to reach a root-mean square roughness of 1–2 nm. The diamond grain size at this side of the wafer amounts to 50–100 nm.

2.2. MBE growth of (Sc,Al)N

By using PAMBE, we have successfully prepared high-quality $\text{Sc}_x\text{Al}_{1-x}\text{N}$ films on different substrates, including

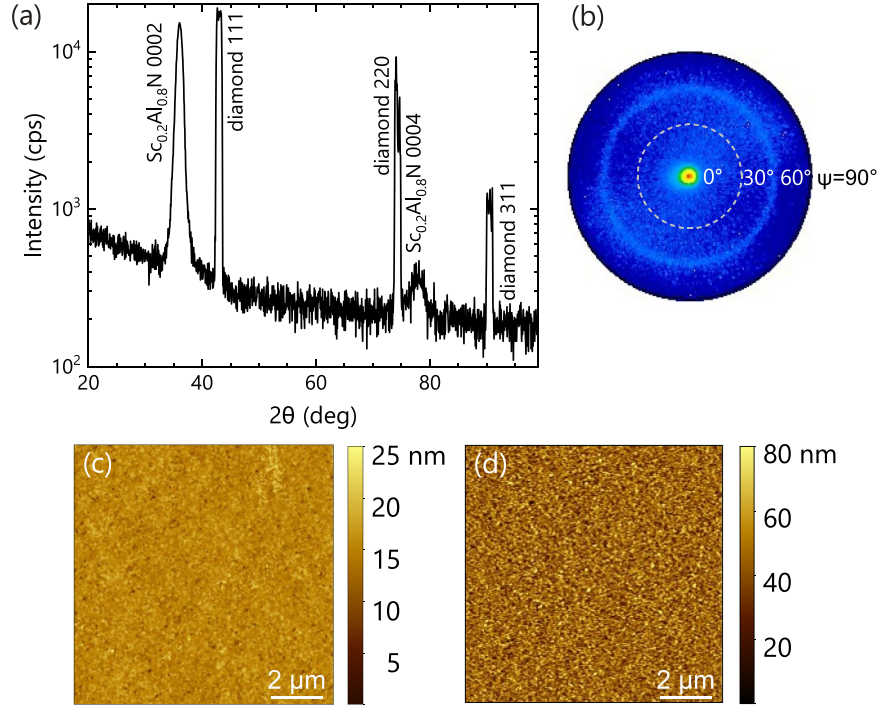


Figure 1. (a) Symmetric $2\theta - \omega$ x-ray diffraction scan of the $\text{Sc}_{0.2}\text{Al}_{0.8}\text{N}$ film grown on polycrystalline diamond substrate. (b) X-ray pole figure of the film recorded with the diffraction angles of the $10\bar{1}1$ reflection ($2\theta = 36.6^\circ$ and $\omega = 18.3^\circ$). The strong reflection at $\psi = 0^\circ$ is from the $\text{Sc}_{0.2}\text{Al}_{0.8}\text{N}$ 0002 reflection since its Bragg angle ($2\theta = 36.0^\circ$ and $\omega \approx 18.0^\circ$) is very close to that of the $10\bar{1}1$ reflection. Atomic force topographs ($10 \times 10 \mu\text{m}^2$) of (c) the diamond substrate and (d) the $\text{Sc}_{0.2}\text{Al}_{0.8}\text{N}$ film. Values of the root-mean square roughness estimated from these topographs are 1.4 and 11.2 nm, respectively.

GaN, AlN and Si [20, 21]. Thin films grown on semi-insulating GaN(0001) templates have been further utilized for high-electron mobility transistors (HEMTs) with electron mobilities exceeding $1000 \text{ cm}^2 \text{ V}^{-1} \text{ s}^{-1}$. We have also found that $\text{Sc}_x\text{Al}_{1-x}\text{N}$ is lattice matched to GaN with $x \approx 0.1$ [20], rather than the most frequently quoted value of 0.18 in literature.

In the present work, we transfer the optimized growth parameters to produce (Sc,Al)N films on polycrystalline diamond/Si templates and free-standing diamond substrates with different grain sizes for SAW devices. All films exhibit a fibre texture with the [0001] c-axis perpendicular to the substrate surface and random in-plane orientation. The out-of-plane orientation distribution of the (Sc,Al)N films was found to be independent on the grain sizes of the diamond substrate, but to strongly depend on its surface morphology. For devices prepared on thin diamond/Si(001) templates, we found that the diamond layers have to exceed a certain thickness to ensure efficient energy confinement and enhanced wave propagation near the surface where the device operates. Hence, we focus in all what follows on films prepared on $150 \mu\text{m}$ thick free-standing diamond wafers.

For the SAW measurements, we prepared 700 nm-thick $\text{Sc}_{0.2}\text{Al}_{0.8}\text{N}$ films on free-standing diamond substrates. To minimize the effects of the diamond surface, the films were grown on the smooth side of the wafers (as described above). The film thickness was chosen to maximize the electromechanical coupling coefficient k_{eff}^2 for the Sezawa mode at $\lambda_{\text{SAW}} =$

$1 \mu\text{m}$ based on calculation. The films were grown at a temperature of 800°C using otherwise the same growth parameters as previously described in [20].

Figure 1(a) shows the $2\theta - \omega$ x-ray diffraction scan (Philips Panalytical X'Pert PRO MRD) of the $\text{Sc}_{0.2}\text{Al}_{0.8}\text{N}$ film grown on a free-standing diamond substrate, performed with open detector without any receiving slit. Besides the reflections related to polycrystalline diamond, there are only reflections related to $\text{Sc}_{0.2}\text{Al}_{0.8}\text{N}$ with {0001} surface orientation. To investigate the in-plane relationship between the film and the polycrystalline substrate, a pole figure around the $\text{Sc}_{0.2}\text{Al}_{0.8}\text{N}$ $10\bar{1}1$ reflection has been recorded, using the respective diffraction angles of $2\theta = 36.6^\circ$ and $\omega = 18.3^\circ$. As shown in figure 1(b), a ring pattern is observed at $\psi = 60^\circ$ that corresponds to the $10\bar{1}1$ reflection of $\text{Sc}_{0.2}\text{Al}_{0.8}\text{N}$. These results reveal that the $\text{Sc}_{0.2}\text{Al}_{0.8}\text{N}$ film is not polycrystalline, but uniaxially textured with the [0001] direction perpendicular to the substrate surface and random in-plane orientation. Apparently, the lattice mismatch between $\text{Sc}_{0.2}\text{Al}_{0.8}\text{N}$ and diamond is too high ($\approx 30\%$) for an epitaxial relation between the two materials, and the growth is columnar, similar to the textured growth of GaN on amorphous substrates [22]. The out-of-plane orientation distribution is examined by recording x-ray rocking curves of the 0002 reflection, which yield a full-width at half maximum of $4^\circ - 4.5^\circ$. As the columns nucleate with their [0001] direction perpendicular to the substrate surface, this width is determined by the waviness of this surface. Figure 1(c) shows an atomic force topograph

(Dimension Edge, Bruker) of the free-standing diamond surface, revealing the substantial roughness and waviness even after extensive chemo-mechanical polishing due to the presence of grains with different orientations, and the extreme hardness of diamond. The surface of the $\text{Sc}_{0.2}\text{Al}_{0.8}\text{N}$ film (figure 1(d)) is even rougher than the substrate because of the tilt of neighbouring columns, the low diffusion length of Sc and Al adatoms under N-rich growth conditions, and the progressive roughening of different regions with further growth.

3. RF characterization of SAWs

The uniaxial texture of the $\text{Sc}_{0.2}\text{Al}_{0.8}\text{N}$ films on diamond allows us to access the piezoelectric nature of the films and thus the excitation of SAWs. To this end, we fabricated a series of single-finger IDTs ranging between $\lambda_{\text{SAW}} = 0.8$ to $3.4 \mu\text{m}$. The electrodes were defined by electron-beam lithography and metallised with a stack of Ti/Al/Ti with 10/50/10 nm thickness (figure 2(a)). In figure 2(b) we show the sample surface investigated under the scanning electron microscope (SEM). The surface exhibits star-shaped features, whose sizes correspond to the grain size of the diamond substrate. The different orientations of the micro-facets in the diamond result in a slight tilt of the *c*-axis of the (Sc,Al)N columns. This morphology is also transferred onto the metallised IDTs.

Figure 3 shows exemplary S-parameter measurements of delay lines formed by opposing IDTs. The S_{11} and S_{21} parameters of the delay line with $\lambda_{\text{SAW}} = 1.7 \mu\text{m}$, 75 pairs of fingers, an aperture of $40\lambda_{\text{SAW}}$ and a gap of $10\lambda_{\text{SAW}}$ is shown in figures 3(a) and (b), respectively. In figures 3(c) and (d) we plot the corresponding parameters for the delay line with $\lambda_{\text{SAW}} = 1 \mu\text{m}$, 80 pairs of fingers an aperture of $68\lambda_{\text{SAW}}$ and a gap of $150\lambda_{\text{SAW}}$.

Multiple significant SAW resonances are observed for the S_{11} parameter in figure 3(a). For the first two modes, namely, the M0 (Rayleigh) mode and the M1 (Sezawa) mode, the size of the dip exceeds 20 dB. Strong resonances are again observed in the S_{21} parameter (figure 3(b)). The signal level for the two modes reach about -30 dB in the GHz range albeit the delay. Both the S_{11} and S_{21} parameters indicate strong piezoelectric coupling. As a result of the shorter λ_{SAW} , the M0 and M1 modes appear at higher frequencies in figure 3(c), again with sizeable dips. The corresponding S_{21} parameter shown in figure 3(d) is lower in signal level due to the much longer delay distance.

The presented S_{21} parameter shows the combined effect of different loss mechanisms. An important contributor among them is the propagation loss, which is expected to play a significant role considering the surface waviness and roughness. As discussed in section 2.2, the $\text{Sc}_{0.2}\text{Al}_{0.8}\text{N}$ film is columnar with its *c*-axis oriented perpendicular to the substrate whereas the in-plane orientation is random. The film is thus textured despite the polycrystalline nature of the diamond substrate. For *c*-plane wurtzite nitrides the phase velocity is homogeneous in-plane and SAWs are mainly affected by the orientational spread of the $\langle 0001 \rangle$ direction. The tilt of columns, determined

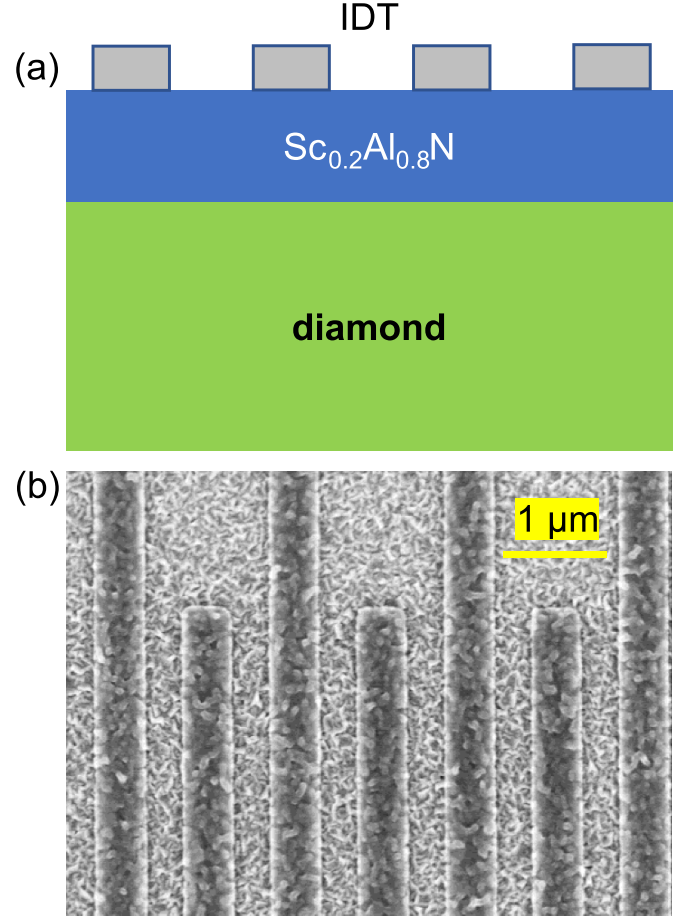


Figure 2. (a) Schematics of the sample layout. (b) Scanning electron micrograph of the surface of the completed sample.

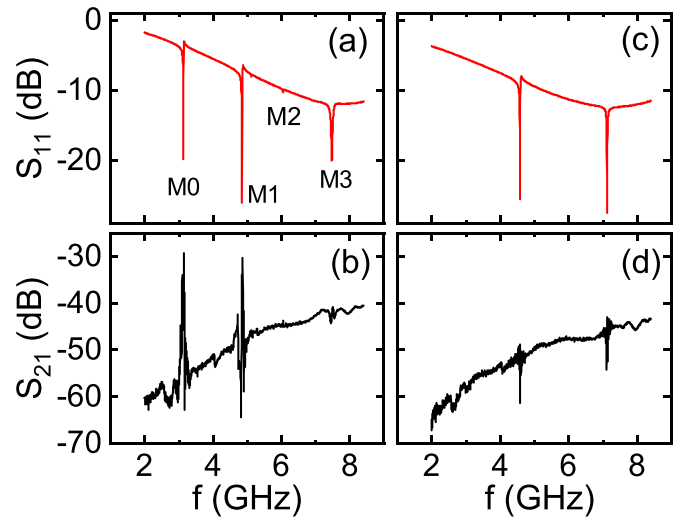


Figure 3. S-parameter measurement for delay lines with (a), (b) $\lambda_{\text{SAW}} = 1.7 \mu\text{m}$, $10\lambda_{\text{SAW}}$ spacing and (c), (d) $\lambda_{\text{SAW}} = 1 \mu\text{m}$, $150\lambda_{\text{SAW}}$ spacing.

by the waviness of the diamond surface, results in SAW scattering at the boundary. Meanwhile, the progressive roughness of the $\text{Sc}_{0.2}\text{Al}_{0.8}\text{N}$ film perturbs the phase velocity and also causes scattering. Therefore, the measured propagation loss

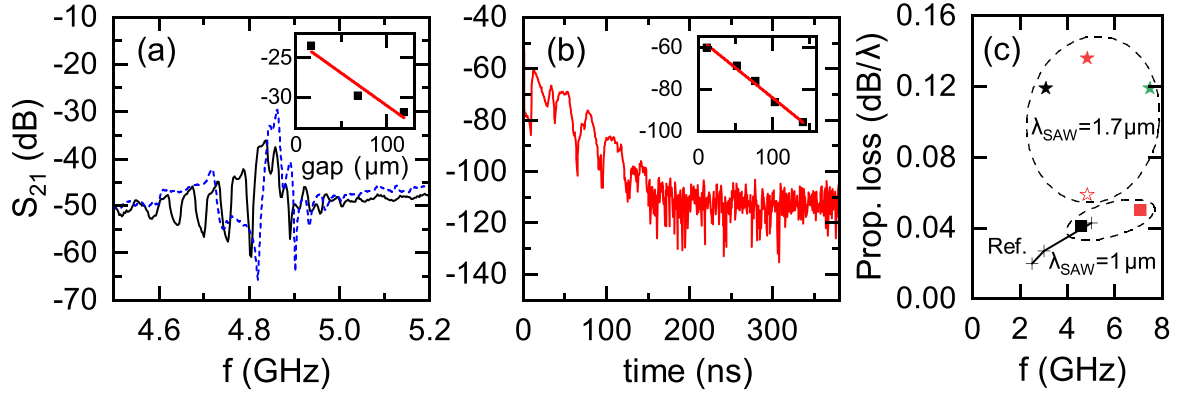


Figure 4. (a) S_{21} for $10 \lambda_{\text{SAW}}$ (blue, dashed line) vs. $70 \lambda_{\text{SAW}}$ spacing. Corrected peak values for different spacing gaps are used to extract the propagation loss (inset). (b) Time-domain echoes of S_{21} for a delay line with $40 \lambda_{\text{SAW}}$ spacing, $\lambda_{\text{SAW}} = 1.7 \mu\text{m}$. Inset: extraction of the propagation loss using the peak values in time. (c) Propagation loss vs. frequency. Filled symbol: extracted with different spacing; hollow symbol: with echoes. Connected cross: from [9].

is a combined effect of the waviness of the substrate and the roughness of the film. In [9] the propagation loss was found to depend on the diamond grain size, neglecting the surface quality of the ZnO film. In this work the surface of the $\text{Sc}_{0.2}\text{Al}_{0.8}\text{N}$ film is expected to play a bigger role than the substrate surface, especially for the lower order SAW modes, confined closer to the surface of the $\text{Sc}_{0.2}\text{Al}_{0.8}\text{N}$ film.

The first method to determine the propagation loss is to measure the S_{21} peak height for delay lines with different gaps, after the correction of return losses for different IDTs. As shown in figure 4(a) for the M1 (Sezawa) mode of a delay line of $\lambda_{\text{SAW}} = 1.7 \mu\text{m}$, longer delay (black) results in a reduced peak compared to the shorter delay (blue). In the inset of figure 4(a), the peak values for three different gaps are plotted and a linear fit is used to determine the propagation loss. The second method consists in probing the echoes in the time domain, assuming that most of the SAWs are reflected at the IDT, as shown in figure 4(b) for the same mode with $40 \lambda_{\text{SAW}}$ spacing. The peak values for each echo are read off and again a linear fit is used to extract the slope, shown in the inset.

The extracted propagation loss for different frequencies is summarized in figure 4(c) (black: M0, red: M1, and green: M3). Filled symbols are values extracted with different gaps and the hollow star symbol is deduced from the echo method. Considering the spectral fluctuation and the device-to-device variations that can be difficult to correct, the echo method (hollow star symbol) is more accurate but requires multiple recordable echoes. For comparison, the result for 500 nm polycrystalline-diamond grain size from [9] on $\text{SiO}_2/\text{ZnO}/\text{diamond}$ is plotted as connected cross symbol. The propagation loss for the Rayleigh mode, $\lambda_{\text{SAW}} = 1 \mu\text{m}$ is very similar to values reported in [9]. The Sezawa mode shows a low propagation loss of $0.05 \text{ dB}/\lambda_{\text{SAW}}$ even above 7 GHz. For $\lambda_{\text{SAW}} = 1.7 \mu\text{m}$ the extracted propagation loss is generally higher, with the exception of the data point extracted with the echo method. If considered in $\text{dB } \mu\text{m}^{-1}$ instead of dB/λ , the propagation loss of the two λ_{SAW} -families are comparable.

4. Frequency modes and electromechanical coupling coefficient: measurement vs. calculation

In figure 5(a), we summarize the detected frequency modes in terms of the nominal phase velocity vs. the relative thickness, i.e. the film thickness h normalized by the wavelength λ_{SAW} for the first 4 modes, labelled as M0, M1, M2 and M3. Their respective mode shapes, manifested as the total displacement, are shown in figure 5(b). The C++ based numerical calculation relies on the differential equations for the propagation of acoustic modes, using the transfer matrix procedure to include multiple layers. More information about the numerical technique can be found in ‘appendix. Numerical Simulations’ of [23].

The elastic constants used here for different materials are summarized in table 1. The elastic constants C_{ij} and the piezoelectric coefficients e_{ij} in C m^{-2} , $e_{15} = -0.3189$, $e_{31} = -0.7216$ and $e_{33} = 2.472$, are calculated following the equations for $\text{Sc}_x\text{Al}_{1-x}\text{N}$ in [17]. The density is 3525 kg m^{-3} . To better fit the experimental data obtained from the $\text{Sc}_{0.2}\text{Al}_{0.8}\text{N}/\text{diamond}$ structure, we have used the parameters calculated for $\text{Sc}_{0.35}\text{Al}_{0.65}\text{N}$ in [17]. In fact, Caro *et al.*’s calculations are based on a weaker dependence of the a lattice constants on x than we have measured [20, 21]. Specifically, their value of a for $\text{Sc}_{0.18}\text{Al}_{0.82}\text{N}$ is comparable to the one we have measured for $\text{Sc}_{0.1}\text{Al}_{0.9}\text{N}$ [20, 21]. Substituting Al with Sc lowers the phase velocities. The mass-loading effect of the IDT, which further lowers the velocities, is simulated by a ‘non-conductive’, uniform Al (2700 kg m^{-3}) layer of 70 nm with C_{ij} from [24]. The elastic constants C_{ij} and density of 3515 kg m^{-3} for diamond used here are from [6].

In figure 5(a), the experimental data (solid symbol) agree well with the calculation (cross connected by dashed line). We identify four significant modes labelled M0 (black), M1 (red), M2 (blue) and M3 (green). The M0 mode corresponds to the commonly studied Rayleigh mode (black), whose curve display the trend that for very small values of h/λ_{SAW} , the nominal phase velocity approaches the Rayleigh velocity in the

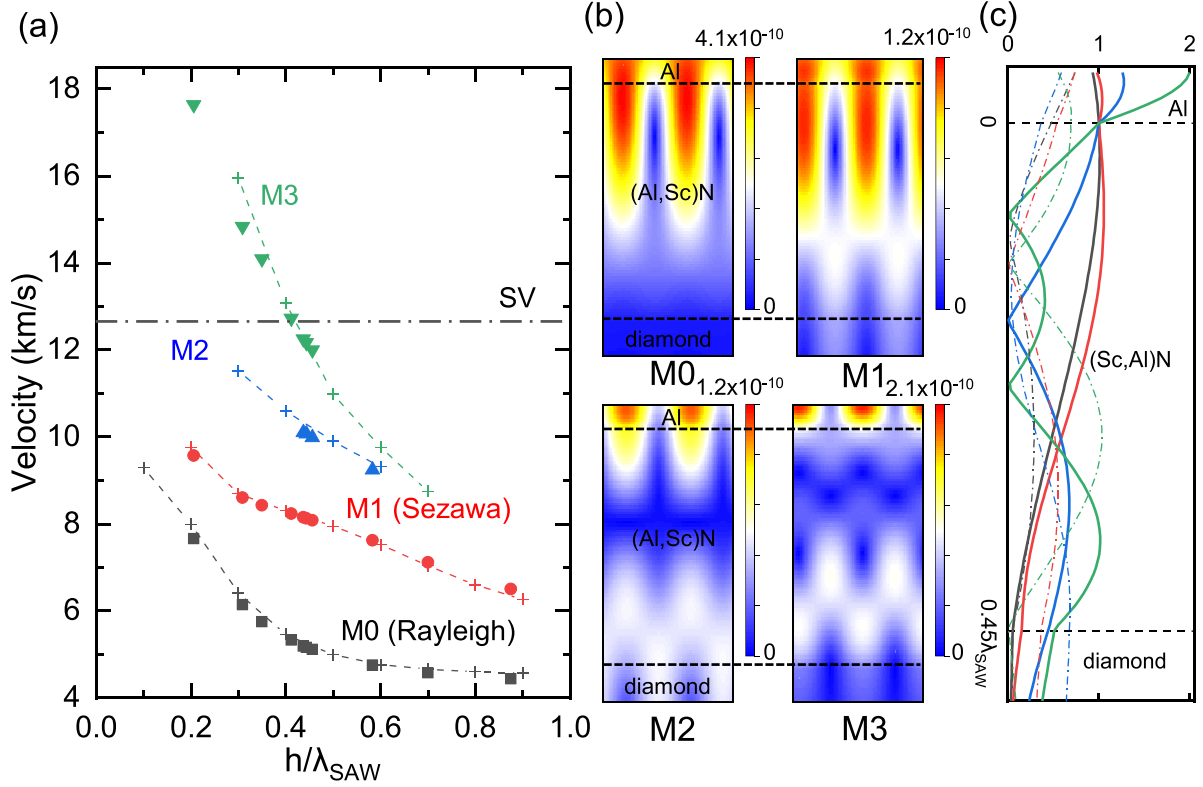


Figure 5. (a) Nominal phase velocity of the experimental SAW resonances (solid symbols) and the theoretically calculated (dashed lines) ones as a function of the normalized thickness. The horizontal line shows the shear vertical (SV) wave velocity in diamond. (b) Calculated total displacement for $h/\lambda_{\text{SAW}} = 0.45$ showing the mode shape for the M0–M3 modes. The range of x -axis is $1 \lambda_{\text{SAW}}$. (c) Vertical cross sections of (b) normalized to the value at the Al/(Sc,Al)N interface for peaks (solid) and valleys (dot–dash) at this interface, same colour coding as in (a).

Table 1. Elastic constants for numerical simulations.

Modulus	Sc _{0.35} Al _{0.65} N [17]	Al [24]	diamond [6]
C_{11}	322.1	111.3	1079
C_{12}	148	59.1	124
C_{13}	136.9		
C_{33}	218.9		
C_{44}	108	26.1	578

substrate material (diamond). As h/λ_{SAW} increases, the velocity drops and becomes asymptotic to the Rayleigh velocity in the (Sc,Al)N film. The M1 mode corresponds to the first Sezawa mode, unique to the ‘slow-on-fast’ structures, with (Sc,Al)N being the film and diamond the substrate, defined as ‘layer’ and ‘substrate’, respectively by Farnell and Adler [25]. Theoretically, the phase velocity of M1 and higher modes cannot exceed that of the shear-vertical (SV, indicated by the horizontal line) wave in diamond. Numerically, above this cutoff the modes have a finite, non-zero determinant. However, since we have observed some of these modes in the experiment, we still treat them as quasi-solutions and include them in figure 5(a). Their leaky nature can be seen, for example, in the much smaller peak around 7.5 GHz in the S_{21} parameter, as shown in figure 3(b).

We also plot the horizontal and depth profile of the calculated total displacement in figure 5(b) for the four modes

at $h/\lambda_{\text{SAW}} = 0.45$ to illustrate the respective mode shapes. In figure 5(c) we show vertical cross sections of figure 5(b) normalized to the value at the Al/(Sc,Al)N interface for peaks (solid) and valleys (dot–dash) along this interface. The M0 mode exhibits typical Rayleigh-wave profile similar to that of free surface, as the black solid line decays with depth, drops to $1/2$ at $0.27\lambda_{\text{SAW}}$ and both the solid and dot–dash tails become negligible in the diamond substrate. The solid curve of M1 mode (red) shows similar trend to M0, however the dot–dash curve is significantly revived at around $0.33\lambda_{\text{SAW}}$. The sinusoidal nature [25] becomes more apparent for the higher modes M2 (blue) and M3 (green), the latter forming a third maximum at a depth of $0.37\lambda_{\text{SAW}}$ (solid green). It can be seen that for the higher modes M1–M3 the elastic energy is shifted away from the Al/(Sc,Al)N interface and carried in the (Sc,Al)N film itself and the penetration into the diamond substrate becomes significant.

After identifying the different modes, we investigate their respective k_{eff}^2 . In a simplified case, k_{eff}^2 can be related to the series resonance f_s and parallel resonance f_p of the BvD model [26, 27] using

$$k_{\text{eff}}^2 = \frac{\frac{\pi}{2} \frac{f_s}{f_p}}{\tan \frac{\pi}{2} \frac{f_s}{f_p}} \approx \frac{\pi^2 f_p - f_s}{2 f_p + f_s}. \quad (1)$$

For very large quality factors Q , f_s and f_p can be directly read off as the extrema from the measured impedance $|Z|$ or admittance $|Y|$ of the resonator. However, for finite Q this is no longer accurate, normally leading to an overestimation of k_{eff}^2 .

To acquire a more accurate estimation, we perform a fit using the modified BvD model illustrated by the inset of figure 6(a). We include a series resistor R_{ser} and a series inductor L_{ser} determined by the peripheral circuit. The acoustic branch is modelled by the acoustic resistor R_a , acoustic capacitor C_a and acoustic inductor L_a . The capacitor in the extra branch C_s is contributed by the geometric capacitor of the IDT C_{geo} and the extra capacitance from the peripheral circuit C_{ex} . We first fit (solid lines) the background of the Y-parameter data (dots) by fixing R_a to a very large value, keeping the acoustic branch open, and providing an initial guess (dashed lines), as shown in figure 6(a) for an IDT with $\lambda_{\text{SAW}} = 1.7 \mu\text{m}$. In a second step we use the R_{ser} , L_{ser} and C_s obtained from the previous step to fit components from the acoustic branches, covering the frequency sub-range of one specific mode. Shown in figure 6(b) is a fit for the encircled M1 (Sezawa) mode in figure 6(a). The fitted Q-factor for the M0, M1 and M3 modes are 424, 394 and 127 (M2, being too weak, is ignored), respectively.

Here, we calculate C_{geo} using the dimensions of the IDTs together with a dielectric constant of 8.85 for (Sc,Al)N. Now, k_{eff}^2 can be evaluated using R_a and the IDT reactance X_{geo} as derived by Smith *et al* [28]:

$$k_{\text{eff}}^2 = \frac{\pi}{4N} \frac{R_a}{X_{\text{geo}}} \equiv k_S^2, \quad (2)$$

where $X_{\text{geo}} = 2\pi f_s C_{\text{geo}}$, and N is the number of finger pairs. This method is not restricted to high values of Q .

In figure 7(a), we plot the coupling coefficient extracted from the fit to the measured data using equation (2) vs. the normalized thickness. We ignore the weak M2 mode in figure 7(d). The numerical calculation of the theoretical coupling coefficient k^2 , by comparing open-circuited and short-circuited velocities, is shown in figure 7(b) surfaces with 70 nm of Al (uniform). The extracted k_S^2 deviate from the calculation. In particular, the expected high coupling coefficient of the M1 (Sezawa) mode is not observed. Instead the M0 and M1 modes have rather similar coupling coefficients, around 1%. Reported values for k_{eff}^2 of the Sezawa mode in AlN/diamond range between 0.1 to 1.4% [11, 12, 29]. For (Sc,Al)N the value is typically enhanced to approximately 3%–6% [30], as summarized in [14]. Note that k_{eff}^2 extracted using the read-off method generally yields a larger value for moderate and low Q 's. A few examples from different devices from our measurements are shown in table 2. The calculated

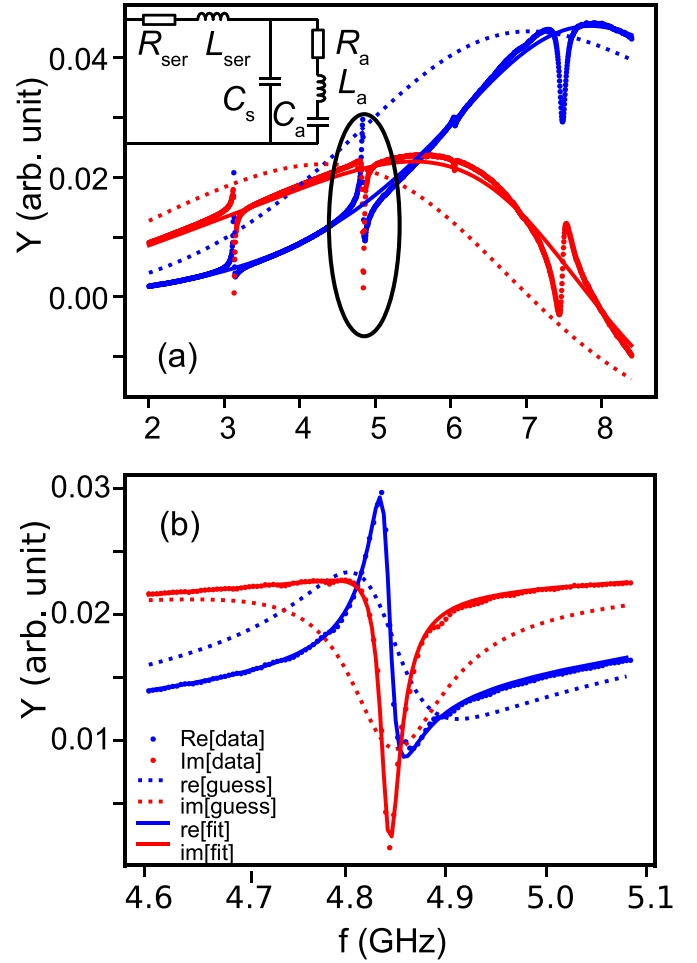


Figure 6. (a) Modified BvD fit of the Y-parameter for the background, $\lambda_{\text{SAW}} = 1.7 \mu\text{m}$. Blue/red: real/imaginary part. Inset: modified BvD model used for the fit. (b) A subsequent fit for the acoustic resonance (M1 mode, encircled in (a)) at 4.83 GHz.

thickness dependence is also not significant in the measurement. Surprisingly, despite being somewhat leaky, the M3 mode shows rather strong coupling, with k_S^2 exceeding 5%. We have not found previous reports of high piezoelectric coupling corresponding to this mode.

To understand this behaviour we resort to the mode shapes illustrated in figures 5(b) and (c). In the case of the M1 (Sezawa) mode, the broad region of maximum total displacement covers the metal/(Sc,Al)N interface. As a result, the Sezawa mode might suffer from the roughness at the surface of the (Sc,Al)N film, originating from the roughness and waviness of the diamond substrate and amplified during PAMBE growth. In contrast, the M3 mode has the nature of a higher Sezawa mode whose first maximum is shifted away from the metal/(Sc,Al)N interface. The second and third maxima (solid green) is shifted to $0.16\lambda_{\text{SAW}}$ and $0.37\lambda_{\text{SAW}}$, respectively inside the (Sc,Al)N film, also avoiding the interface. Consequently, this mode may be less sensitive to the roughness and waviness at this interface. Note that due to the roughness of the sample surface, which can limit the efficiency of SAW generation, the exerted k_{eff}^2 is a lower bound of the theoretically

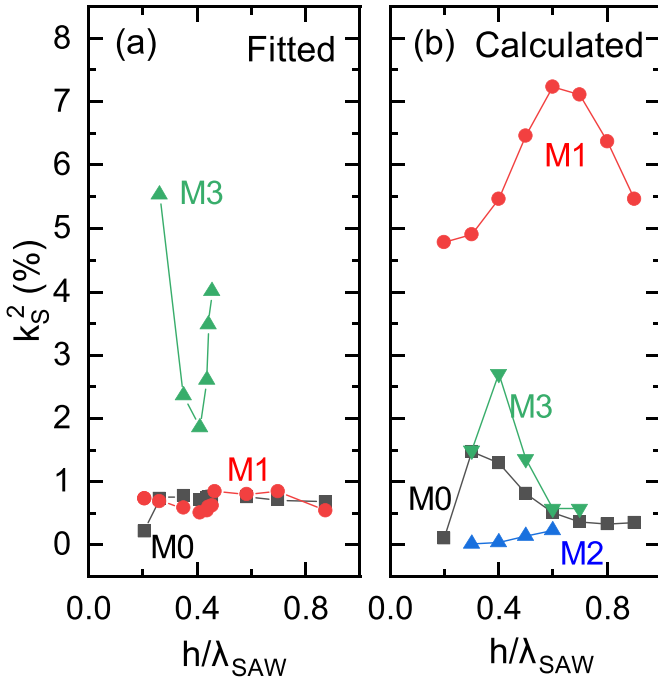


Figure 7. (a) Electromechanical coupling coefficient k_s^2 extracted from the fitted R_a vs. normalized thickness. (b) Calculated k^2 with uniform electrodes.

Table 2. Comparison of k_{eff}^2 extracted by two different methods.

Mode	h/λ_{SAW}	k_s^2	k_{eff}^2 , readoff
M0	0.35	1.1	0.78
M1	0.7	0.85	2.4
M3	0.26	5.5	8.4

possible values. Besides, the dependence on the relative metal thickness h_m/λ_{SAW} is neglected here, which can contribute to the discrepancy. A finite-element approach will be more accurate in modelling the IDTs.

5. Conclusion

In conclusion, we have demonstrated the possibility of growing (Sc,Al)N thin films using PAMBE on free-standing, polycrystalline diamond as well as the generation of multiple SAW modes in the multiple-GHz range. The S-parameters as well as the propagation losses have been characterized. The tracing of the measured SAW velocity as a function of the relative film thickness agrees well with the theoretical calculation. Furthermore, we extract the electromechanical coupling coefficient from the measurement for an extended range of normalized thickness. A deviation from the theoretical expectation is observed, revealing the complication in SAW-generation efficiency. The results confirm the potential of this material combination and contribute to the foundation for potential application in telecommunication.

Data availability statement

The data cannot be made publicly available upon publication because the cost of preparing, depositing and hosting the data would be prohibitive within the terms of this research project. The data that support the findings of this study are available upon reasonable request from the authors.

Acknowledgment

We thank Nicole Bickel, Walid Anders and Abbes Tahraoui for sample processing, and Yukihiro Takagaki for useful discussions.

ORCID iDs

Mingyun Yuan <https://orcid.org/0000-0002-7627-3916>
 Duc V Dinh <https://orcid.org/0000-0002-5915-3365>
 Soumen Mandal <https://orcid.org/0000-0001-8912-1439>
 Oliver A Williams <https://orcid.org/0000-0002-7210-3004>
 Zhuohui Chen <https://orcid.org/0000-0002-7903-8460>
 Oliver Brandt <https://orcid.org/0000-0002-9503-5729>
 Paulo V Santos <https://orcid.org/0000-0002-0218-8030>

References

- [1] Takagaki Y, Santos P V, Wiebicke E, Brandt O, Schönherr H-P and Ploog K H 2002 Superhigh frequency surface-acoustic-wave transducers using AlN layers grown on SiC substrates *Appl. Phys. Lett.* **81** 2538
- [2] Akiyama M, Kano K and Teshigahara A 2009 Influence of growth temperature and scandium concentration on piezoelectric response of scandium aluminum nitride alloy thin films *Appl. Phys. Lett.* **95** 1–4
- [3] Wang W, Mayrhofer P M, He X, Gillinger M, Ye Z, Wang X, Bittner A, Schmid U and Luo J K 2014 High performance AlScN thin film based surface acoustic wave devices with large electromechanical coupling coefficient *Appl. Phys. Lett.* **105** 133502
- [4] Hao Z, Park M, Gyu Kim D, Clark A, Dargis R, Zhu H and Ansari A 2019 Single crystalline ScAlN surface acoustic wave resonators with large figure of merit ($Q \times k$) 2019 *IEEE MTT-S Int. Microwave Symp. Digest* pp 786–9
- [5] Ding A et al 2020 Enhanced electromechanical coupling in SAW resonators based on sputtered non-polar $\text{Al}_{0.77}\text{Sc}_{0.23}\text{N}$ ($11\bar{2}$) thin films *Appl. Phys. Lett.* **116** 101903
- [6] McSkimin H J and Andreatch P Jr 1972 Elastic moduli of diamond as a function of pressure and temperature *J. Appl. Phys.* **43** 2944–8
- [7] Deger C, Born E, Angerer H, Ambacher O, Stutzmann M, Hornsteiner J, Riha E and Fischerauer G 1998 Sound velocity of $\text{Al}_x\text{Ga}_{1-x}\text{N}$ thin films obtained by surface acoustic-wave measurements *Appl. Phys. Lett.* **72** 2400
- [8] Andrew Golter D, Oo T, Amezcua M, Lekavicius I, Stewart K A and Wang H 2016 Coupling a surface acoustic wave to an electron spin in diamond via a dark state *Phys. Rev. X* **6** 041060
- [9] Uemura T, Fujii S, Kitabayashi H, Itakura K, Hachigo A, Nakahata H, Shikata S, Ishibashi K and Imai T 2002 Low loss diamond SAW devices by small grain size polycrystalline diamond *Proc. IEEE Ultrasonics Symp.* vol 1 pp 431–4

- [10] Fujii S, Shikata S, Uemura T, Nakahata H and Harima H 2005 Effect of crystalline quality of diamond film to the propagation loss of surface acoustic wave devices *IEEE Trans. Ultrason. Ferroelectr. Freq. Control* **52** 1817–22
- [11] Benetti M, Cannatà D, Di Pietrantonio F and Verona E 2005 Growth of AlN piezoelectric film on diamond for high-frequency surface acoustic wave devices *IEEE Trans. Ultrason. Ferroelectr. Freq. Control* **52** 1806–11
- [12] Elmazria O, El Hakiki M, Mortet V, Assouar B M, Nesládek M, Vanecek M, Bergonzo P and Alnot P 2004 Effect of diamond nucleation process on propagation losses of AlN/diamond SAW filter *IEEE Trans. Ultrason. Ferroelectr. Freq. Control* **51** 1704–8
- [13] Sinusia Lozano M, Chen Z, Williams O A and Iriarte G F 2018 Temperature characteristics of SAW resonators on $\text{Sc}_{0.26}\text{Al}_{0.74}\text{N}$ /polycrystalline diamond heterostructures *Smart Mater. Struct.* **27** 075015
- [14] Sinusia Lozano M, Fernández-García L, López-Romero D, Williams O A and Iriarte G F 2022 SAW resonators and filters based on $\text{Sc}_{0.43}\text{Al}_{0.57}\text{N}$ on Single Crystal and Polycrystalline Diamond *Micromachines* **13** 1–9
- [15] Wang L, Chen S, Zhang J, Zhou J, Yang C, Chen Y and Duan H 2018 High performance 33.7 GHz surface acoustic wave nanotransducers based on AlScN/diamond/Si layered structures *Appl. Phys. Lett.* **113** 093503
- [16] Park M, Hao Z, Dargis R, Clark A and Ansari A 2020 Epitaxial aluminum scandium nitride super high frequency acoustic resonators *J. Microelectromech. Syst.* **29** 490–8
- [17] Caro M A, Zhang S, Riekkinen T, Ylilammi M, Moram M A, Lopez-Acevedo O, Molarius J and Laurila T 2015 Piezoelectric coefficients and spontaneous polarization of ScAlN *J. Phys.: Condens. Matter* **27** 245901
- [18] Mandal S 2021 Nucleation of diamond films on heterogeneous substrates: a review *RSC Adv.* **11** 10159–82
- [19] Williams O A 2011 Nanocrystalline diamond *Diam. Relat. Mater.* **20** 621–40
- [20] Dinh D V, Lähnemann J, Geelhaar L and Brandt O 2023 Lattice parameters of $\text{Sc}_x\text{Al}_{1-x}\text{N}$ layers grown on GaN(0001) by plasma-assisted molecular beam epitaxy *Appl. Phys. Lett.* **122** 152103
- [21] Dinh D V, Chen Z and Brandt O Crack-free $\text{Sc}_x\text{Al}_{1-x}\text{N}$ ($0 \leq x \leq 0.35$) layers grown on Si(111) by plasma-assisted molecular beam epitaxy (unpublished)
- [22] Stoica T, Sutter E, Meijers R J, Debnath R K, Calarco R, Lüth H and Grützmacher D 2008 Interface and wetting layer effect on the catalyst-free nucleation and growth of GaN nanowires *Small* **4** 751–4
- [23] Takagaki Y, Santos P V, Wiebicke E, Brandt O, Schönherr H-P and Ploog K H 2002 Guided propagation of surface acoustic waves in GaN and AlN films grown on 4H-SiC(0001) substrates *Phys. Rev. B* **66** 155439
- [24] Slobodnik A J, Conway E D and Delmonico R T 1973 *Microwave Acoustics Handbook, Vol. 3: Bulk Wave Velocities* (National Technical Information Service, US Department of Commerce)
- [25] Farnell G W and Adler E L 1972 Elastic wave propagation in thin layers *Physical Acoustics* vol 9 (Academic) ch 2, pp 35–127
- [26] Naik R S, Lutsky J J, Reif R and Sodini C G 1998 Electromechanical coupling constant extraction of thin-film piezoelectric materials using a bulk acoustic wave resonator *IEEE Trans. Ultrason. Ferroelectr. Freq. Control* **45** 257–63
- [27] Hashimoto K-Y 2009 *RF Bulk Acoustic Wave Filters for Communications* (Artech House Microwave Library)
- [28] Smith W R, Gerard H M, Collins J H, Reeder T M and Shaw H J 1969 Analysis of interdigital surface wave transducers by use of an equivalent circuit model *IEEE Trans. Microwave Theory Tech.* **17** 856–64
- [29] Assouar M B, Elmazria O, Kirsch P, Alnot P, Mortet V and Tiusan C 2007 High-frequency surface acoustic wave devices based on AlN/diamond layered structure realized using e-beam lithography *J. Appl. Phys.* **101** 114507
- [30] Ya Hashimoto K, Fujii T, Sato S, Omori T, Ahn C, Teshigahara A, Kano K, Umezawa H and Ichi Shikata S 2012 High Q surface acoustic wave resonators in 2-3 GHz range using ScAlN/single crystalline diamond structure *IEEE Int. Ultrasonics Symp., IUS* pp 1–4